

Revealing the promotion/inhibition mechanism of CO_3^{2-} in the oriented electrocatalytic conversion of ethane to 2-propanol and acetone

Yubo Zhang, Saifei Wang*, Xuan Liu, Jiaqi Lv, Xuerui Hao, Erhong Duan*

National Joint Local Engineering Research Center for Volatile Organic Compounds and Odorous Pollution Control, School of Environmental Science and Engineering, Hebei University of Science and Technology, 26th Yuxiang Street, Shijiazhuang, Hebei, China

ARTICLE INFO

Keywords:

Electrochemical ethane oxidation
Ethane conversion in room temperature
Ethane converted to 2-propanol
Side reaction competition
 CO_3^{2-} adsorption mechanism on lattice O/O defects

ABSTRACT

Ethane conversion is an important industrial process, however, the conversion of ethane into high value-added chemicals at room temperature has rarely been studied. Herein, a $\text{NaCo}_2\text{O}_4/\text{CeO}_2$ has been fabricated to convert ethane to 2-propanol and acetone, in which Na was introduced in Co_3O_4 to change the coordination environment of Co and produce more lattice O on NaCo_2O_4 . The highest selectivity of acetone could reach to 89 %. In the reaction process, the promotion effect of CO_3^{2-} and the competition between CO_3^{2-} OR and C_2H_6 OR was also confirmed. After changing Co_3O_4 to NaCo_2O_4 , the lattice O increased and acted as active site of C_2H_6 oxidation reaction. Furthermore, the defects on CeO_2 made primary effects on CO_3^{2-} oxidation reaction. By combining the ATR-FTIR spectra and DFT calculation, the two pathways of CO_3^{2-} adsorption was simulated to infer the mechanism of reaction promoting process.

1. Introduction

As the second most abundant gas in natural gas, it is easy to cause resource waste if ethane is converted to CO_2 directly. Besides, excessive emissions of CO_2 can also cause greenhouse effects and lead to global warming [1]. Therefore, it is considered to convert alkane to other high-valued chemical products for meeting the demand of storage and application. Dogu and his coworkers doped La and Cl into SrTiO_3 to make $\text{La}_{0.2}\text{Sr}_{0.8}\text{TiO}_{3\pm\delta}\text{Cl}_\delta$ for converting ethane to ethylene by electrocatalysis [2]. Zhang and his team used $\text{BaCe}_{0.7}\text{Zr}_{0.1}\text{Y}_{0.1}\text{Yb}_{0.1}\text{O}_{3-\delta}$ to electrochemical dehydrogenation of ethane to ethylene in a solid oxide electrolyzer. Furthermore, the H^+ generated from ethane was also transported to cathode and combined with CO_2 . In this way, the CO_2 could also be reduced to CO [3]. Although ethane conversion involves the dehydrogenation of ethane to ethylene at high temperatures traditionally [4], the storage and transportation of gas product C_2H_4 is still a problem that needs to be solved. In this case, electrocatalytic conversion at room temperature is needed to meet the demands of resources reasonable utilization.

Transition metal oxides are always used as an active phase in electrochemical conversion process. Jong and coworkers provided an accessible pathway for methane diffusion on the catalyst by modifying Co_3O_4 onto ZrO_2 , thereby reducing the onset potential of methane oxidation to convert methane to ethanol [5]. Except for Co_3O_4 , ZrO_2 was

also anchored on the strong active catalyst Cu_2O (111), ZrO_2 promote charge redistribution and create a quick electron transfer network to support a higher methane conversion capability [6]. In addition to consider suitable catalysts, electrocatalytic conversion of methane also requires selecting appropriate electrolytes to promote the chemical reaction and practical applications. Introducing free radicals into the reaction system can promote the smooth progress of the reaction. A molecular catalyst of vanadium (V)-oxo dimer was used to convert methane in 98 % H_2SO_4 , which yields cation radicals on the sulfonic ligand that selectively activate CH_4 [7]. Furthermore, NiO/ZnO shell-/core nanorod catalyst in 0.5 mol/L Na_2CO_3 solution can convert CH_4 to ethanol [8]. More importantly, this study proved that the O in CO_3^{2-} finally became the O in ethanol by using $\text{C}^{16}\text{O}_3^{2-}$ and $\text{C}^{18}\text{O}_3^{2-}$. In addition, Jaehyun Lee and coworkers analyzed the mechanism that the O in CO_3^{2-} became the OH in ethanol by DFT calculation [9]. Therefore, the competition between target reactant and side reactions should also be discussed in the electrochemical reaction process.

In this case, it is important to design reasonable electrocatalysts since side reactions in electrochemical reaction process is the key factor to determine the catalysts performance. Li and coworkers manufactured iron-nickel hydroxide (Fe-Ni-OH) nanosheet to convert CH_4 in 0.1 mol/L NaOH , which was found to produce $\text{Ni}^{III}\text{OOH}$ to serve as active sites in reaction process [10]. Besides, the competition between OER and CH_4 oxidation reaction was also found, leading to choose the most active and

* Corresponding authors.



selectivity catalysis among all samples. To control the competition between OER and ethanol oxidation reaction (EOR), Wang and his team use Chemisorbed octadecylamine ligands to create an layer at the ultrathin Ni(OH)₂ nanosheets surface to improve EOR activity and selectivity by promoting alcohol diffusion and adsorption in an alkaline solution [11]. Furthermore, Geng and his coworkers manufactured a immobilized Ag pyrazole (AgPz) molecular catalyst to control the strong *OH binding energy to promote the H₂O dissociate into *OH, then the AgPz reversible changed to AgPz-Hvac with a weak *OH binding energy, which promote the Propylene convert to Propylene Glycol [12]. The reversible changing process is the main reason to avoid the strong *OH binding energy hinder the propylene oxidation reaction.

In this study, Na atoms were doped in the spinel type metal oxide Co₃O₄ to change the chemical valence state and coordination environment of Co in order to obtain a higher ethane oxidation performance. To adjust the performance of the CO₃²⁻ oxidation reaction, the content of CeO₂ was changed in NaCo₂O₄/CeO₂ by adding different qualities of Co (NO₃)₂·6H₂O. To explore the Co₃O₄ being changed by Na during the preparing process, TG and XRD was used to detect the intermediate products in different calcination temperature. By comparing the CO₃²⁻ oxidation reaction (CO₃²⁻ OR) and C₂H₆ oxidation reaction (C₂H₆ OR) performance of catalysts and combining the XPS results, the active site of C₂H₆OR was confirmed as the lattice O on NaCo₂O₄ and the CO₃²⁻ OR mainly occurred on the defects of catalysts. Besides, after confirming the best potential and the most suitable Na₂CO₃ solution concentration by detecting products after 6 h, the pathway of ethane conversion to 2-propanol was inferred by testing in situ attenuated total reflectance Fourier transform infrared (ATR-FTIR) experiments. Finally, DFT calculation was used to confirm the competition between C₂H₆ OR and CO₃²⁻ OR and detect the possible mechanism of CO₃²⁻ OR promotion process.

2. Experimental

2.1. Preparation of two-phase composite catalysts xNaCo₂O₄/CeO₂

Using solution combustion method to produce xNaCo₂O₄/CeO₂. To produce NaCo₂O₄/CeO₂, dissolve the metal precursors Ce(NO₃)₃·6H₂O (0.868 g) and Co(NO₃)₂·6H₂O (0.582 g) with the molar ratio of Co: Ce=1:1 in DI water, the molar ratio of Co: Ce=2:1 and 4:1 were also calculated to produce 2NaCo₂O₄/CeO₂ and 4NaCo₂O₄/CeO₂ using the same method mentioned next. Under continuous stirring, dissolve EDTA-2Na (1.5 g) and citric acid (1.5 g) in the above mixture in turn (The Na: Co: Ce=4.4:1:1 in NaCo₂O₄/CeO₂, the quantity of EDTA-2Na was fixed). After stirring for 20 min, adjust the pH to 8 with ammonia water (NH₃·H₂O). Then, stir the mixture at 80 °C to obtain a purple solution, roast to 280 °C for 1 h. Remove and grind after cooling down, annealed to 800 °C for 2 h. In addition, pure NaCo₂O₄ and CeO₂ was also synthesized in same method for comparison. The EDTA-2Na was replaced to EDTA to produce Co₃O₄/CeO₂ with the same process above.

2.2. Electrocatalytic performance measurements

The electrocatalytic performance of xNaCo₂O₄/CeO₂ was tested by linear sweep voltammetry (LSV) and electrochemical impedance spectroscopy (EIS) measurements in a three-electrode system using electrochemical workstation (DH 7003). The glassy carbon electrode (0.07 cm²) was used as the working electrode (WE), Pt foil as the counter electrode (CE), Ag/AgCl electrode as the reference electrode (RE). All electrocatalytic performance was tested in 0.5 mol/L Na₂CO₃ solution.

Mix 2 mg of catalyst with 0.68 mL of water, 0.3 mL ethanol and 0.02 mL 5 % Nafion solution, ultrasonic vibration for 20 min, and then drop 16 μL onto the surface of the working electrode. Before testing LSV, Ar was purged for 15 min to eliminate other gases in the system. After LSV was tested, C₂H₆ was also purged for 20 min to create a saturated reactants condition. Then EIS was tested in 1.7 V(vs.RHE) which is the

onset potential of CO₃²⁻ OR for these catalysts, and the range of frequency was from 100,000 Hz to 0.1 Hz with a voltage amplitude of 5 mV.

The electrochemical ethane conversion was tested by Chronoamperometry (CA) in a three-electrode system. The Pt foil and Ag/AgCl electrode were used as the counter electrode and reference electrode, respectively. The working electrode was made by carbon cloth for 1×1.5 cm and make sure that 1 cm² carbon cloth was in solution. To make ink solution, 8 mg catalyst was dispersed in a mixed solution including 1.5 mL water and 1.5 mL ethanol by ultrasonic machine for 20 min. Add 30 μL 5 % Nafion solution on carbon cloth after it was washed by water and dried on 40 °C. After assembling the three electrodes, add 23 mL Na₂CO₃ solution on electrolytic cell. LSV was tested in Ar and C₂H₆-saturated solution by bubbling for 15 min. The potential was from 0.9 to 2.3 V(vs.RHE) and scan rate was 5 mV/s. Finally, CA was used to convert ethane for 6 h by continuous blowing C₂H₆.

Tafel slope was calculated by formula below, the data was obtained from the results of current density and potential in LSV curves.

$$\eta = a + b \cdot \lg i_l$$

In this formula, η is the potential and we chose 2.0–2.4 V(vs.RHE) as the range of calculation, as the products was occurred in 2.1 V(vs.RHE). The i is the current density. a is the constant and we use segmented fitting to obtain the slope as the b in formula.

2.3. Physical characterization and instruments

The X-ray diffraction (XRD) characterization of the materials was performed on a D/Max-2500 (Rigaku Corporation, Japan) using Cu K α radiation ($\lambda = 0.15406$ nm, 40 kV and 150 mA) with a scanning range of 10°–80° and a scanning speed of 10°/min. High-resolution TEM (JEOL 2010 F and FEI Talos F200S) was used to analyse the structure and element distribution for these catalysts. The XPS (Thermo Scientific Nexsa) was used to detect the chemical valence state of all catalysts. The values of binding energies were calibrated with the C 1 s peak of contaminant carbon at 284.80 eV. Thermogravimetric analysis (TGA) was used to detect the changing temperature of catalysts with the heating ratio of 5°C/min. EPR for O defects detection was on the Bruker A300, the condition was: central magnetic field 3500.00 G; The sweeping width was 150.00 G; The sweeping time was 30.00 seconds; The microwave power was 3.99 mW; The modulation amplitude was 1.000 G; The conversion time was 40.0 ms, 9.854854 GHz.

2.4. Product analysis

To investigate products after ethane conversion, Gas chromatography (GC 7820 A, Agilent Technologies, USA) with a flame ionization detector (FID) and a HT-PPFA column was used for product qualitative and quantitative analysis. The injection temperature was set to 300 °C. For the FID, a flow of 400 mL/min synthetic air, 40 mL/min H₂ fuel, and 20 mL/min N₂ make-up was applied. To identify the product, possible organic matter 2-propanol, 1-propanol, ethanol, methanol and acetone were also mixed with Na₂CO₃ solution and tested by GC, respectively. After that, 0.15 mL sample was mixed with 0.25 mL D₂O and recorded by ¹H NMR (Bruker AVANCE NEO 500 M) for qualitative analysis. The out gas was tested by Gas chromatography (GC 7920, Beijing Aulight Co. Ltd), which is equipped with FID and SE-54 column (50 m×0.32 mm×0.5μm). The injection temperature was set to 150 °C. The temperature of column box was 70 °C.

2.5. In situ ATR-FTIR experiments

To detect the intermediate products during the reaction process, in situ attenuated total reflectance Fourier transform infrared (ATR-FTIR) spectroscopy (Nicolet iS50, Thermo Fisher, USA). The H-type interchangeable membrane Raman in-situ electrochemical cell was used

where applying the catalyst onto the silicon wafer as the working electrode, Ag/AgCl electrode as reference electrode. The Pt foil was in another side of the cell and act as counter electrode.

2.6. In situ EPR experiments

The 2Na₂O₄/CeO₂ catalyst was used as the working electrode (WE), Pt foil as the counter electrode (CE), Ag/AgCl electrode as the reference electrode (RE). After introducing ethane gas into the solution for 15 min, conducting conversion experiments in 2.3 V (vs.RHE) under the condition of continuous low flow rate introduction of ethane. 5,5-dimethyl-1-pyrroline N-oxide (DMPO) was used as a spin-trapping reagent for conducting EPR experiments. In situ EPR for detection was on the Bruker A300, the condition was: central magnetic field 3500.00 G; The sweeping width was 150.00 G; The sweeping time was 30.00 seconds; The microwave power was 3.99 mW; The modulation amplitude was 1.000 G; The conversion time was 40.0 ms, 9.854854 GHz.

2.7. Computational details

All the calculations are performed in the framework of the density functional theory with the projector augmented plane-wave method, as implemented in the Vienna ab initio simulation package [13]. The generalized gradient approximation proposed by Perdew, Burke, and Ernzerhof is selected for the exchange-correlation potential [14]. The cut-off energy for plane wave is set to 400 eV. The energy criterion is set to 10–5 eV in iterative solution of the Kohn-Sham equation. All the structures are relaxed until the residual forces on the atoms have

declined to less than 0.05 eV/Å.

To obtain the adsorption performance of different reactants at various interface sites, the adsorption energy (E_{ads}) is calculated as follows:

$$E_{ads} = E_{*adsorbate} - E_* - E_{adsorbate}$$

Where $E_{*adsorbate}$ and E_* are the total energy of the surface with and without adsorbates, respectively. $E_{adsorbate}$ represents the total energy of the adsorbate in the gas phase.

3. Results and discussion

3.1. Characterization of xNa₂O₄/CeO₂

The XRD spectrum of the xNa₂O₄/CeO₂ are shown in Fig. 1a, the peaks at 28.5°, 47.4° and 56.3°, corresponding to (111), (220) and (311) planes of CeO₂ (PDF#43-1002), respectively [15]. Peaks at 16.3°, 33.1° and 50.0° correspond to (002), (004) and (104) planes of Na₂O₄ (PDF#27-0682) are also identified [16]. No other oxides related to Na are found in the XRD spectrum, except for Na₂O₄. TEM image of 2Na₂O₄/CeO₂ (Fig. 1b) illustrates that two-phase catalyst are composite through the manufacturing process. The TEM image of CeO₂ and Na₂O₄ from Fig. S1 and Fig. S2 could help to identify two species, the large sheet like structure is Na₂O₄ and the spherical species are CeO₂. Comparing with single phase, the morphology of 2Na₂O₄/CeO₂ are similar comparing with CeO₂ and Na₂O₄ in TEM, which indicates that there was no phase change occurred between CeO₂ and Na₂O₄ during the production process. The Na₂O₄/CeO₂ and 4Na₂O₄/CeO₂ image

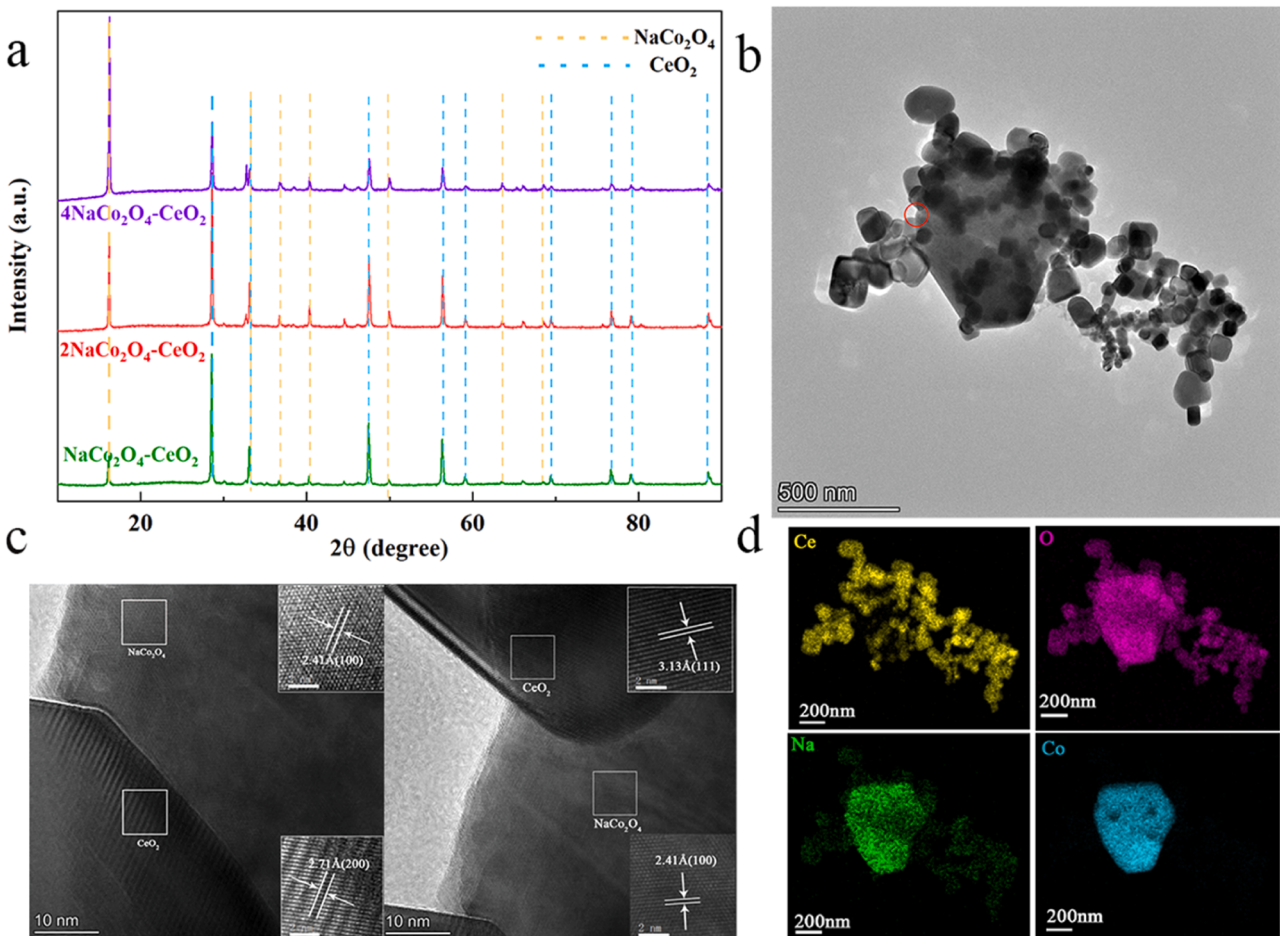


Fig. 1. Structural characterizations of xNa₂O₄/CeO₂. (a) XRD patterns of xNa₂O₄/CeO₂. (b) TEM image of 2Na₂O₄/CeO₂. (c) TEM images for 2Na₂O₄/CeO₂ from the red circle in Fig. 1b. (d) EDS element mapping of 2Na₂O₄/CeO₂.

could find in **Fig. S3** and **Fig. S4**, the morphology of them also stay the same with $2\text{NaCo}_2\text{O}_4/\text{CeO}_2$, illustrates that the change of $\text{Co}(\text{NO}_3)_2 \cdot 6\text{H}_2\text{O}$ only alter the proportion of catalysts. For $2\text{NaCo}_2\text{O}_4/\text{CeO}_2$, TEM image shows the (111) and (200) crystal planes exposed to CeO_2 and the (100) crystal planes corresponding to NaCo_2O_4 (**Fig. 1c**) [17, 18]. The EDS results of $2\text{NaCo}_2\text{O}_4/\text{CeO}_2$ also prove this inference (**Fig. 1d**). Furthermore, the EDS image not only shows the distribution of Na in the center of the catalysts, but also shows in the CeO_2 , which indicates that the Na was distributed on all the catalysts in the beginning of catalysts manufacturing process.

3.2. The electro-performance of catalysts toward C_2H_6 OR

To test the C_2H_6 OR performance of ethane, the LSV curves for five catalysts dispensed on carbonate electrolyte in C_2H_6 and Ar-saturated Na_2CO_3 solution are shown in **Fig. 2a**. The current density difference between two curves in the same potential is the key parameter to evaluate the capability of C_2H_6 OR (**Fig. 2b**) [6]. The $2\text{NaCo}_2\text{O}_4/\text{CeO}_2$ exhibits the highest current density difference in three composite catalysts. In addition, the NaCo_2O_4 and CeO_2 both exhibits the C_2H_6 OR capability. Besides, comparing with the current density contrast of two single-phase catalysts, the current density difference of CeO_2 is lower than that of NaCo_2O_4 . This result not only shows high C_2H_6 oxide capability, but also reveals strong synergistic effect between NaCo_2O_4 and CeO_2 . Except current density, good conductivity could also reflect the performance of catalysts [19]. EIS was tested in 1.7 V (vs.RHE) as the EIS results shows that CeO_2 has the worst electronic conduction and highest ohmic resistance, NaCo_2O_4 is on the contrary (**Fig. 2c**). According to the ICP (**Table S1**) and TEM results, even if $2\text{NaCo}_2\text{O}_4/\text{CeO}_2$ has similar proportion comparing with $4\text{NaCo}_2\text{O}_4/\text{CeO}_2$, the electrochemical performance including electronic conduction and current density is the worst in three catalysts, which could attribute to agglomerated in the process of preparation identified by TEM graph. For $2\text{NaCo}_2\text{O}_4/\text{CeO}_2$ and $4\text{NaCo}_2\text{O}_4/\text{CeO}_2$, NaCo_2O_4 could promote electronic conductivity, also, CeO_2 is distributed in the surface of NaCo_2O_4 .

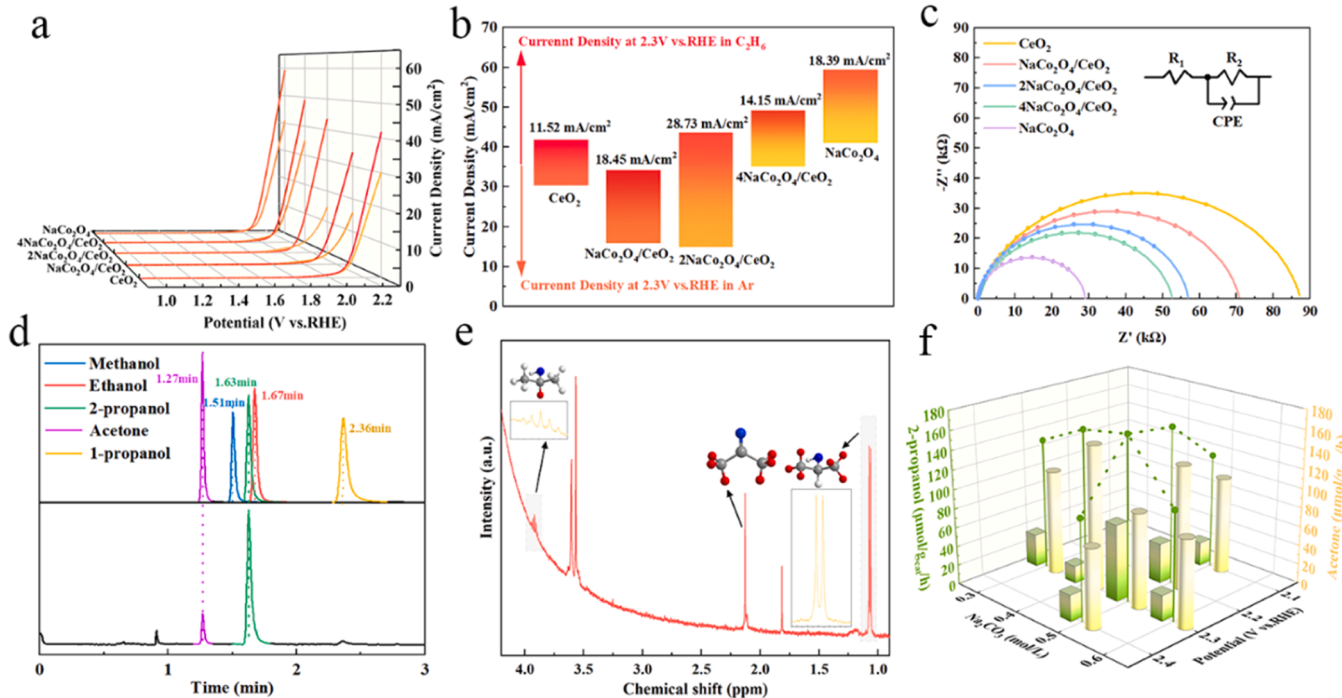


Fig. 2. (a) LSV curves of five catalysts in both Ar and C_2H_6 -saturated Na_2CO_3 solution. (b) the current density difference in 2.3 V(vs.RHE) of five catalysts. (c) EIS results of five catalysts in 1.7 V(vs.RHE), form 100,000 Hz to 0.1 Hz. (d) GC results of peak time including product and possible products sampling in GC. (e) ${}^1\text{H}$ NMR results of C_2H_6 OR in 2.3 V(vs.RHE) after 6 h in 0.5 mol/L Na_2CO_3 solution. (f) Product concentration from 2.1 V(vs.RHE) to 2.4 V(vs.RHE) in 0.5 mol/L Na_2CO_3 solution and the concentration from 0.3 mol/L to 0.6 mol/L Na_2CO_3 solution in 2.3 V(vs.RHE).

3.4. Catalyst synthesis mechanism and active sites

To further explain the process of the formation of the catalysts, the pre-calcined products and catalysts in different temperature of $2\text{NaCo}_2\text{O}_4/\text{CeO}_2$ was tested by TG and XRD (Fig. 3a, b). The pre-calcined products and the temperature less than 500°C composited by Co_3O_4 and CeO_2 are denoted as $2\text{Co}_3\text{O}_4/\text{CeO}_2$ and $2\text{Co}_3\text{O}_4/\text{CeO}_2(500^\circ\text{C})$. After increasing temperature from 500°C to 700°C , the main products denoted as $2\text{Na}_{0.6}\text{CoO}_2/\text{CeO}_2$ are $\text{Na}_{0.6}\text{CoO}_2$ and CeO_2 . Finally, the products became $2\text{NaCo}_2\text{O}_4/\text{CeO}_2$. By comparing the XPS results of $2\text{Co}_3\text{O}_4/\text{CeO}_2(500^\circ\text{C})$ and $2\text{NaCo}_2\text{O}_4/\text{CeO}_2$. The binding energy of Co 2p, O 1s and Na 1s are shown in Fig. 3c and Fig. 3d, Fig. S9 and Table S3. The binding energy of Ce 3d had no obvious change in the process of calcine. Combining with XRD results, CeO_2 was not influenced by Na. For $2\text{Co}_3\text{O}_4/\text{CeO}_2$, it could be seen that the Co 2p_{3/2} peak can be fitted into Co^{3+} and Co^{2+} components at the binding energy of 779.1 eV and 780.8 eV . The Co 2p_{3/2} peak of $2\text{NaCo}_2\text{O}_4/\text{CeO}_2$ in 778.7 eV and 780.4 eV could be attribute to Co^{3+} and Co^{2+} [22,23]. A shift of 0.4 eV occurred after introducing Na in Co_3O_4 , which results in redistribution of interfacial charges. Furthermore, the ratio of $\text{Co}^{3+}/\text{Co}^{2+}$ increased from 1.47 to 2.62 (Table S3) after Na was introduced, which illustrates that with the increasing of the temperature, there was a great change occurred in Co_3O_4 and new phase produced. According to the crystal structure of NaCo_2O_4 , the increase of Co^{3+} represents more lattice O produced and the Co^{2+} could attribute to O defects in the surface of NaCo_2O_4 . Besides, the O 1s of $2\text{Co}_3\text{O}_4/\text{CeO}_2$ and $2\text{NaCo}_2\text{O}_4/\text{CeO}_2$ can be deconvoluted into four peaks. The peaks of 528.9 eV and 528.5 eV could attribute to lattice O, the peaks in 530.7 eV and 530.4 eV could bind to O defect. Furthermore, comparing with $2\text{Co}_3\text{O}_4/\text{CeO}_2$ and $2\text{NaCo}_2\text{O}_4/\text{CeO}_2$, the ratio of lattice O/O defects have a great raise from 1.07 to 1.75 . The introduce of Na recrystallized Co_3O_4 to form a new phase, thereby increasing the amount of lattice oxygen and reduced the content of O defects.

To investigate the resource of Na, the EDTA-2Na was exchanged to EDTA in the manufacturing process of $2\text{NaCo}_2\text{O}_4/\text{CeO}_2$. The XRD pattern was shown in Fig. S10, the final product was $\text{Co}_3\text{O}_4/\text{CeO}_2$. From

these results, it is confirmed that Na is dispersed in products because of the EDTA-2Na. Furthermore, to investigate the existing state of Na, the XPS results of Na 1s between $2\text{Co}_3\text{O}_4/\text{CeO}_2(500^\circ\text{C})$ and NaCo_2O_4 are compared, there is only 0.1 eV shift in binding energy, however, there are no Na oxide exist in XRD pattern in Fig. 3b. Finally, from the EDS results of $2\text{NaCo}_2\text{O}_4/\text{CeO}_2$ in Fig. 1(d), the Na in CeO_2 was dispersed but not gathered as Co or Ce elements. In this case, the Na are amorphous form in low temperature (280°C , 500°C). These two catalysts $2\text{Co}_3\text{O}_4/\text{CeO}_2(500^\circ\text{C})$ and $\text{Co}_3\text{O}_4/\text{CeO}_2$ was also used for C_2H_6 conversion in $2.3\text{ V}(vs.\text{RHE})$, however, there was no product tested by GC.

The XPS results of $2\text{NaCo}_2\text{O}_4/\text{CeO}_2$ are also compared with CeO_2 and NaCo_2O_4 and shown in Fig. S11. The Co 2p_{3/2} peak can be fitted into Co^{3+} and Co^{2+} components at the binding energy of 779.3 eV and 780.8 eV , respectively. According to Table S3, the ratio of $\text{Co}^{3+}/\text{Co}^{2+}$ in $2\text{NaCo}_2\text{O}_4/\text{CeO}_2$ increased comparing with NaCo_2O_4 . Furthermore, the O 1s and Na 1s has changed after the combination of NaCo_2O_4 and CeO_2 . The Na 1s of $2\text{NaCo}_2\text{O}_4/\text{CeO}_2$ also occurs a peak in 1068.8 eV (Fig. S11). The lower binding energy of Na 1s may come from the combination between NaCo_2O_4 and CeO_2 , which could illustrate that the Na not only changed the Co_3O_4 but also connected NaCo_2O_4 and CeO_2 . For O 1s, the ratio of lattice O/O defects in $2\text{NaCo}_2\text{O}_4/\text{CeO}_2$ is more than single-phase, which indicates that it is different in the process of catalysts preparation. If NaCo_2O_4 and CeO_2 are prepared individually, there would be more O defects, however, co synthesis could produce more lattice O. The reason for this phenomenon would indicates that the co-synthesis made more CeO_2 composite with NaCo_2O_4 and covered more defects.

To explore the connection between catalyst changes and electrochemical conversion capability, all catalysts formed in manufacturing process was tested by LSV. At first, $2\text{NaCo}_2\text{O}_4/\text{CeO}_2$ was used to test the LSV curves in different solution and the results are shown in Fig. S12. Comparing with Na_2CO_3 , $0.5\text{ mol/L Na}_2\text{SO}_4$ solution has same concentration of both Na^+ and anion. However, there is a huge gap in current density in $2.3\text{ V}(vs.\text{RHE})$ between two solutions, which means the ion concentration in solution is not a determining factor of current density. Besides, the $0.5\text{ mol/L Na}_2\text{CO}_3$ solution was tested by Acidimeter, the

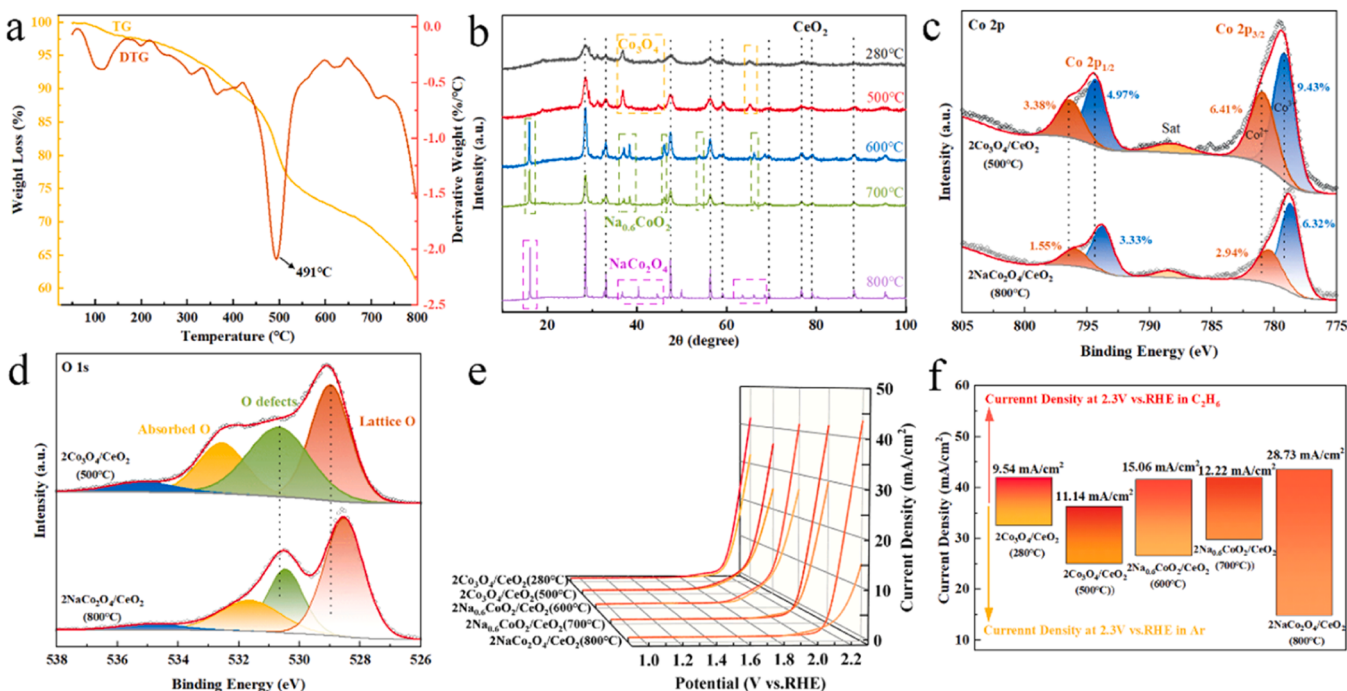


Fig. 3. (a) TG curves of $2\text{NaCo}_2\text{O}_4/\text{CeO}_2$ at a heating rate of 5°C . (b) XRD patterns of $2\text{NaCo}_2\text{O}_4/\text{CeO}_2$ precursor calcined in different temperatures. (c) XPS results of Co 2p spectra for $2\text{Co}_3\text{O}_4/\text{CeO}_2$ and $2\text{NaCo}_2\text{O}_4/\text{CeO}_2$. (d) XPS results O 1s spectra for $2\text{Co}_3\text{O}_4/\text{CeO}_2$ and $2\text{NaCo}_2\text{O}_4/\text{CeO}_2$. (e) LSV curves of $2\text{NaCo}_2\text{O}_4/\text{CeO}_2$ precursor calcined in different temperatures. (f) the current density difference in $2.3\text{ V}(vs.\text{RHE})$ of precursors.

result was pH=11.4. The NaOH solution in the same pH was made and tested to investigate whether the OER dominated in reaction process, the LSV curve was almost same comparing with Na_2SO_4 solution, illustrates that OER is not the main reaction in Na_2CO_3 solution. Therefore, the LSV results tested after Ar-saturated is the CO_3^{2-} OR and convert it to O^{2-} and CO_2 [6,19]. After using the $2\text{NaCo}_2\text{O}_4/\text{CeO}_2$ by chronoamperometry (CA) to convert ethane in different solutions (Fig. S13), it was found that only Na_2CO_3 solution exists products, which demonstrates that O^{2-} is essential in ethane conversion. Furthermore, the current density difference of five catalysts in different calcination temperatures in 2.3 V(vs. RHE) are shown in Fig. 3e and Fig. 3f, the CO_3^{2-} OR capability of $2\text{NaCo}_2\text{O}_4/\text{CeO}_2$ is the worst. Combining with the XPS results of O 1 s, Co 2p and product results of five catalysts after C_2H_6 OR process, the ratio of O defects also declined, which indicates that O defects are the main active site for CO_3^{2-} OR. To further illustrate the changes in O defects, EPR was also tested, the results are shown in Fig. S14, the O defects became less after $2\text{Co}_3\text{O}_4/\text{CeO}_2$ (500 °C) was changed to $2\text{NaCo}_2\text{O}_4/\text{CeO}_2$. The $2\text{NaCo}_2\text{O}_4/\text{CeO}_2$ also has less defects comparing with $4\text{NaCo}_2\text{O}_4/\text{CeO}_2$, which is corresponding with the amount of production between these two catalysts in 2.3 V(vs.RHE) [24]. Besides, the C_2H_6 OR capability also increased after $2\text{Co}_3\text{O}_4/\text{CeO}_2$ was converted to $2\text{NaCo}_2\text{O}_4/\text{CeO}_2$, through this process, the ratio of $\text{Co}^{3+}/\text{Co}^{2+}$ also increased, which could illustrate that lattice O is the main factor for C_2H_6 OR.

To explore the function of CeO_2 , the substantial differences in the redox properties and CO_3^{2-} OR performances of all catalysts except $\text{NaCo}_2\text{O}_4/\text{CeO}_2$ on glassy carbon electrode are shown by cyclic voltammetry (CV) recorded in 0.5 mol/L Na_2CO_3 solution (Fig. S15). Two sets of pre- CO_3^{2-} OR redox features are observed in $2\text{NaCo}_2\text{O}_4/\text{CeO}_2$, $4\text{NaCo}_2\text{O}_4/\text{CeO}_2$ and NaCo_2O_4 . The redox peaks have no occurrence in CV curves of CeO_2 , which could indicate that the redox peaks in other three catalysts are attribute to NaCo_2O_4 . The reversible processes may be assigned to cobalt redox species involving $\text{Co}^{\text{III}}/\text{Co}^{\text{II}}$ and $\text{Co}^{\text{IV}}/\text{Co}^{\text{III}}$ couples, respectively [25–28]. With the increasing content of CeO_2 , the redox potential of NaCo_2O_4 is also increasing, which could indicate that the CeO_2 could improve the stability of the catalyst by increasing the redox potential of NaCo_2O_4 .

To test the stability of the $2\text{NaCo}_2\text{O}_4/\text{CeO}_2$, the carbon cloth loaded with catalyst was compared before and after 6 h of C_2H_6 conversion. From the XRD pattern in Fig. S16, both NaCo_2O_4 and CeO_2 peaks were declined because of the catalyst was detached. However, there was no change in XRD pattern, which could illustrate that the catalyst is stable. From the XPS results in Fig. S17, there was a small shift occurred after 6 h. There was an increase in the number of lattice O/O defects from 1.75 in origin to $2\text{NaCo}_2\text{O}_4/\text{CeO}_2$ after 6 h. However, the number of $\text{Co}^{3+}/\text{Co}^{2+}$ had a decrease from 2.62 to 1.67, which could attribute to partial damage occurred on the surface of NaCo_2O_4 . The reason may form the O^{2-} produced from CO_3^{2-} . This phenomenon illustrates that the increase of the lattice O most came from the CeO_2 .

As a result, the mechanism of ethane electrocatalytic conversion on catalysts is that the interface between NaCo_2O_4 and CeO_2 created a good environment for the O defects mainly responsible for CO_3^{2-} OR to decline energy barrier for C_2H_6 OR, afterwards, the C_2H_6 was activated by lattice O on $2\text{NaCo}_2\text{O}_4/\text{CeO}_2$ and oxidized through CO_3^{2-} OR.

3.5. The competition of C_2H_6 OR and CO_3^{2-} OR

It is known that CO_3^{2-} is easier to be oxidized comparing with C_2H_6 . In this case, it is vital to explore the competition between C_2H_6 OR and CO_3^{2-} OR. As the results above, the 2-propanol in 2.3 V(vs.RHE) has the most content. To test the competition between CO_3^{2-} OR and C_2H_6 OR and find suitable solution concentration, $2\text{NaCo}_2\text{O}_4/\text{CeO}_2$ was used in 0.1–0.6 mol/L Na_2CO_3 solution at 2.3 V(vs.RHE), the results are also shown in Fig. 2f. The reason for the absence of products at 0.1–0.2 mol/L is that insufficient CO_3^{2-} could not supply enough O^{2-} . The total 2-propanol production is raising from 136.67 to 169.46 $\mu\text{mol/g}_{\text{cat}}/\text{hr}$ with the

increasing solution concentration and suddenly cut down to 111.31 $\mu\text{mol/g}_{\text{cat}}/\text{hr}$ in 0.6 mol/L Na_2CO_3 , this may attribute to excessive CO_3^{2-} suppressed ethane conversion. The highest selectivity of acetone reaches 89 % at 2.3 V(vs.RHE) in 0.4 mol/L Na_2CO_3 solution. The most product yield was at 2.3 V(vs.RHE) in 0.5 mol/L Na_2CO_3 solution. From these results, excessive energy supply and CO_3^{2-} concentration could lead to the competition of two reaction. The CO_3^{2-} OR capability of five catalysts is shown in Fig. S18. The NaCo_2O_4 and CeO_2 have no products may also attribute to high O defects content lead to the excessive competition of CO_3^{2-} OR. Furthermore, this conclusion could also infer that the CO_3^{2-} OR could not convert C_2H_6 individually. The C_2H_6 OR is the synergistic effect of both CO_3^{2-} OR on defects and the lattice O in NaCo_2O_4 . In addition, comparing the Tafel slope of three composite materials after introducing Ar and ethane, the Tafel slope of $2\text{NaCo}_2\text{O}_4/\text{CeO}_2$ and $4\text{NaCo}_2\text{O}_4/\text{CeO}_2$ in Ar indicates that it is more difficult to oxidize CO_3^{2-} in the weak polarized region (Fig. S19–21). As the voltage increases, CO_3^{2-} OR in the strong polar region increases [6]. However, after introducing ethane, the Tafel slope increases, which attribute to more difficulty for chemical reaction as C_2H_6 OR is introduced into the overall reaction process. The Tafel slope of $4\text{NaCo}_2\text{O}_4/\text{CeO}_2$ shows less variation compared to $2\text{NaCo}_2\text{O}_4/\text{CeO}_2$ in the strongly polarized region, indicating that ethane participates less in the overall reaction, corresponding to a lower yield of products at 2.3 V(vs.RHE). For $\text{NaCo}_2\text{O}_4/\text{CeO}_2$, the Tafel slope did not increase in strong polarized region after the addition of ethane, indicating that ethane did not participate in the overall reaction.

To investigate the importance of CO_3^{2-} OR, 10 μL 2-propanol was also added in 0.5 mol/L Na_2SO_4 solution and the result is compared with result in 0.5 mol/L Na_2CO_3 in Fig. S22. The content of acetone in 0.5 mol/L Na_2SO_4 solution has a significant decline comparing with 0.5 mol/L Na_2CO_3 solution, which indicates that the production of acetone is mainly from the effect of CO_3^{2-} OR. In addition, the HER process occurred on counter electrode have no promoting effect on oxidation reaction. This result could also confirm that the CO_3^{2-} OR is the only reaction that promote the process of C_2H_6 OR.

To study the C_2H_6 OR mechanism on the $2\text{NaCo}_2\text{O}_4/\text{CeO}_2$ surface, in situ ATR-FTIR and EPR experiments were carried out to record the intermediate products in the process of producing 2-propanol. Fig. 4a shows the spectra collected in different potentials from 2.1 to 2.3 V(vs. RHE) after reacted 60 min. All three peaks are almost same, which indicates that the reaction process are same even if the potential are different. The bands at 1045 cm^{-1} and 1087 cm^{-1} could be assigned to C-OH and C-O stretching vibration in ethanol [29,30]. Besides, the band in 1365 cm^{-1} and 1179 cm^{-1} are the C-H and C-C deformation vibration of 2-propanol, respectively [31,32]. Afterwards, the band at 1732 cm^{-1} and 1643 cm^{-1} could attribute to C=O stretching vibration of acetaldehyde and symmetric stretching vibration of C=C in C_2H_4 [31,33]. Finally, the band in 2349 cm^{-1} is corresponding to asymmetrical stretching vibration of CO_2 [30]. For band in 2349 cm^{-1} , the intensity of CO_2 is weaker in 2.3 V(vs.RHE) than lower potential. This could be connected to the competition between CO_3^{2-} OR and C_2H_6 OR and the results are same. In 2.3 V(vs.RHE), CO_3^{2-} OR is weaker results in more C_2H_6 OR and the increase of products. It is proved that the 2-propanol appeared in catalyst successfully. Besides, ethanol (C–O, C–C), acetaldehyde (C=O), ethylene (C=C) and CO_2 were detected. These intermediate products recorded in Table 1 may go through further oxidation and serve as the stable intermediate to form the main products.

After confirming 2.3 V(vs.RHE) as the best potential of C_2H_6 OR, time series ATR-FTIR spectra are obtained by fixing the electrode potential at 2.3 V(vs.RHE) and monitoring the spectra changes with reaction time (Fig. 4b). Some characteristic peaks appear (shown in Table 1) after the reaction begins and the intensity gradually grows with time increase. The peaks of CO_2 (2349 cm^{-1}) had a gradual improve before 20 min, which indicates that the CO_3^{2-} OR is the main reaction during this period of time. The band of ethanol in 1045 cm^{-1} and 1087 cm^{-1} was detected after 10 min and accumulating in the rest of

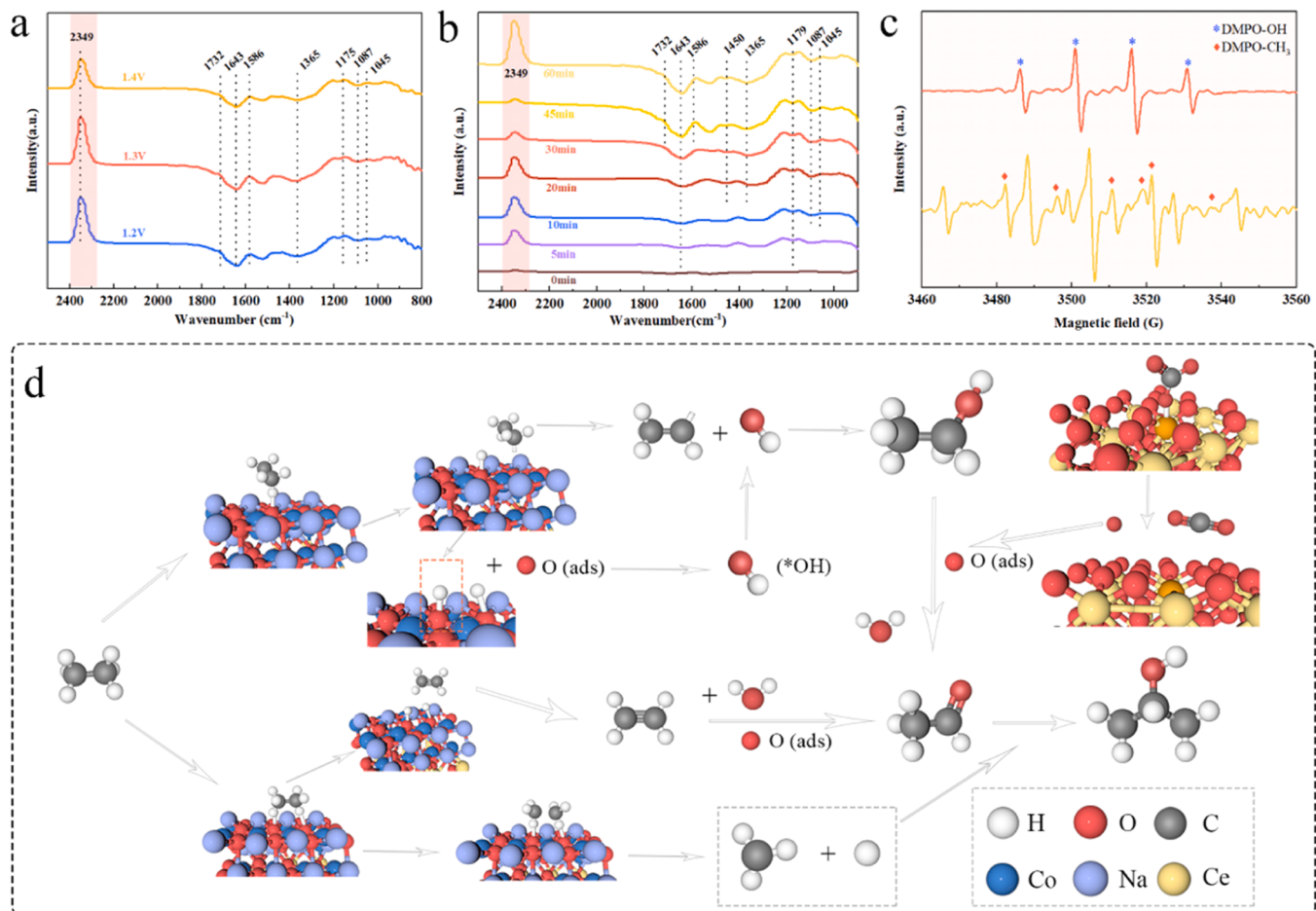


Fig. 4. (a) In situ ATR-FTIR results of 2NaCo₂O₄/CeO₂ in different potential after 1 h. (b) In situ ATR-FTIR results of 2NaCo₂O₄/CeO₂ at 2.3 V(vs.RHE) in different time periods. (c) In situ EPR results of 2NaCo₂O₄/CeO₂ in 2.3 V(vs.RHE). (d) Reaction pathway of C₂H₆ conversion.

Table 1
ATR-FTIR absorbance bands and corresponding band assignments.

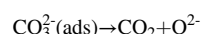
Frequency (cm ⁻¹)	Band assignment
1045	ν (C—OH) in ethanol
1087	ν (C—O) in ethanol
1179	δ (C—C) in 2-propanol
1365	δ_s (CH ₃) in 2-propanol
1643	ν_s (C=C) in ethylene
1732	ν (C=O) in acetaldehyde
2349	ν_{as} (C=C) in CO ₂

time. The 2-propanol band in 1179 cm⁻¹ and 1365 cm⁻¹ occurred after ethanol was found, which could infer that 2-propanol is converted by ethanol as the intermediate. In 30 min and 45 min, as the CO₃²⁻ OR declined, the C₂H₆OR occupied more oxidation processes since the intensity of CO₂ in 2349 cm⁻¹ declined but the intensity of C₂H₄ in 1643 cm⁻¹ increased. In this case, there are two pathways for forming C₂H₄ including C₂H₆ was activated on the surface of NaCo₂O₄ and ethanol was oxidized by O²⁻. After 45 min, the peak of acetaldehyde in 1732 cm⁻¹ was finally detected, which could infer that acetaldehyde was converted by ethanol and C₂H₄ due to O²⁻ oxidation. The reason why acetaldehyde was not occurred in 30 min may attribute to low content caused by insufficient ethanol and C₂H₄. After C₂H₄ was accumulated sufficiently and acetaldehyde occurred, the peak of 2-propanol was also improved. From these results, the rate-limiting step could be inferred as the process that C₂H₄ was converted to acetaldehyde as the direct changing relation between them.

To further investigate the formation process and the catalytic

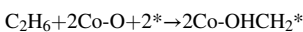
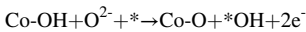
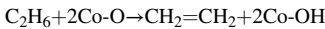
mechanism, 5,5-dimethyl-1-pyrroline N-oxide (DMPO) was used as a spin-trapping reagent for conducting EPR experiments. The ·CH₃ and ·OH was tested in 2.3 V(vs.RHE) after converting C₂H₆ for 15 min. From the EPR results in Fig. 4c, there are ·CH₃ exist in the reaction process [34–36], which could verify that the C-C bond was broken. Besides, from the mechanism that methane conversion to ethanol or 2-propanol, the products originate from the coupling of methyl groups. The ·OH was also tested in the reaction process [37], this could be attributed to the combination of O²⁻ and H from C₂H₆. From the 2-propanol conversion experiment, if the ·OH produced from the counter electrode, the 2-propanol should be converted easily in Na₂SO₄ solution. In this case, the ·OH should have a greater possibility that produced in CO₃²⁻ OR process. This evidence could also explain the formation of ethanol.

Based on the ATR-FTIR spectra and EPR results, combining with the mechanism of adsorbate evolution mechanism (AEM) and the lattice oxygen mechanism (LOM) [38,39]. The process of C₂H₆ OR activation in 2NaCo₂O₄/CeO₂ and the conversion of C₂H₅OH and CH₂=CH₂ are all shown in Fig. 4d. Combining with the mechanism proposed by Jaehyun Lee [9] and the results obtained above, the CO₃²⁻ was combined with the defects of CeO₂ and became CO₂ and O²⁻ [6].

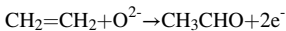


To explore the formation process of CH₂=CH₂. First, it is reported that C₂H₆ could be dehydrogenated to C₂H₄ [2,40]. In this case, The two H in C₂H₆ may combine with two lattice O in Co—O to produce Co—OH and CH₂=CH₂ [41]. Afterwards, the O²⁻ from CO₃²⁻ would combine with Co—OH to produce Co—O and *OH. Also, due to the weaker C—C bond compared with the C—H bond, the C₂H₆ could also be activated by Co—O

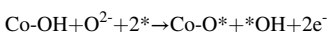
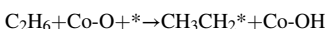
and produce Co-OHCH_2^* [3].



After $\text{CH}_2=\text{CH}_2$ was produced, with the help of O^{2-} and H_2O , the $\text{CH}_2=\text{CH}_2$ could be converted to CH_3CHO easily due to Wacker reaction [42].



For the formation mechanism of $\text{C}_2\text{H}_5\text{OH}$, the most possible way is C_2H_6 activated on catalysts, the C-H bond combined with the lattice O on NaCo_2O_4 to produce Co-OH and CH_3CH_2^* , then the O^{2-} attacked Co-OH to produce C-O and $^*\text{OH}$, finally, the CH_3CH_2^* was combined with $^*\text{OH}$ and synthesized $\text{C}_2\text{H}_5\text{OH}$ [6,8].



It is reported that $\text{C}_2\text{H}_5\text{OH}$ could also be converted to $\text{CH}_2=\text{CH}_2$ by electrocatalysis [33], this could explain the reason that the $\text{CH}_2=\text{CH}_2$ peak is more and more strong in the reaction process.

Finally, the CH_3CHO combined with CH_3^* and H absorbed on Co-O to produce $\text{CH}_3\text{CHOHCH}_3$.



3.6. DFT calculation

To further understand the catalytic activity of the difference between

lattice O and O defects, DFT calculations were conducted by focusing on the energy changes of absorption and reaction of CO_3^{2-} on CeO_2 and NaCo_2O_4 surface. At first, the catalyst model of the $2\text{NaCo}_2\text{O}_4$ (100) and CeO_2 (100) was chosen as the exposed crystal plane and created O defects on both side (Fig. 5a). To explore the different possible adsorption pathway of CO_3^{2-} , one or two O atoms of CO_3^{2-} (Pathway A and B) adsorbed on both NaCo_2O_4 and CeO_2 surface were simulated (Fig. 5b). From Fig. 5c, the CO_3^{2-} adsorption energy (E_{ads}) on CeO_2 was decreased from -4.337 eV to -5.41 eV if two O atoms was absorbed on defects (Pathway B), the E_{ads} on NaCo_2O_4 was also decreased from -6.024 eV to -6.257 eV, which indicates that Pathway B is much easier comparing with Pathway A. These two different adsorption pathway also illustrate that the Pathway B could be the main reason for reaction promotion on CO_3^{2-} OR due to the exposed O(or O^{2-}) on CO_3^{2-} . The other pathway could offer lattice O to activate C_2H_6 and produce CO_2 .

Moreover, both E_{ads} on NaCo_2O_4 are lower than that of CeO_2 , which could illustrate that NaCo_2O_4 has a stronger CO_3^{2-} OR capability. This result is identical to Fig. 2b as the current density of NaCo_2O_4 in CO_3^{2-} OR is higher than CeO_2 . Furthermore, the adsorption reaction could occur on both NaCo_2O_4 and CeO_2 . In this case, the CeO_2 could also participate on CO_3^{2-} OR thereby offer more opportunities for C_2H_6 OR on NaCo_2O_4 surface. In addition, from the in situ ATR-FTIR results, it can be seen that the reason for the decrease in CO_2 intensity at 30 min in Fig. 4c may be due to the temporary occupation of defect sites by oxygen atoms, resulting in a decrease in CO_3^{2-} OR. Meanwhile, the intermediate products also began to accumulate after 30 min, proves that the lattice O accumulated and activated C_2H_6 .

To investigate the competition of CO_3^{2-} between lattice O and O defects, the adsorption energy of CO_3^{2-} on lattice O was also calculated based on the more favorable Pathway B. From Fig. 5c, the E_{ads} on lattice O are both higher than that of O defects. The E_{ads} on the lattice O of NaCo_2O_4 (-4.627 eV) was also lower than Pathway A on O defects (-6.024 eV), which illustrates that defects on NaCo_2O_4 are the main active site for CO_3^{2-} OR. Furthermore, E_{ads} on the lattice O of CeO_2 (-5.209 eV) was even lower than Pathway A on O defects. As a result, the

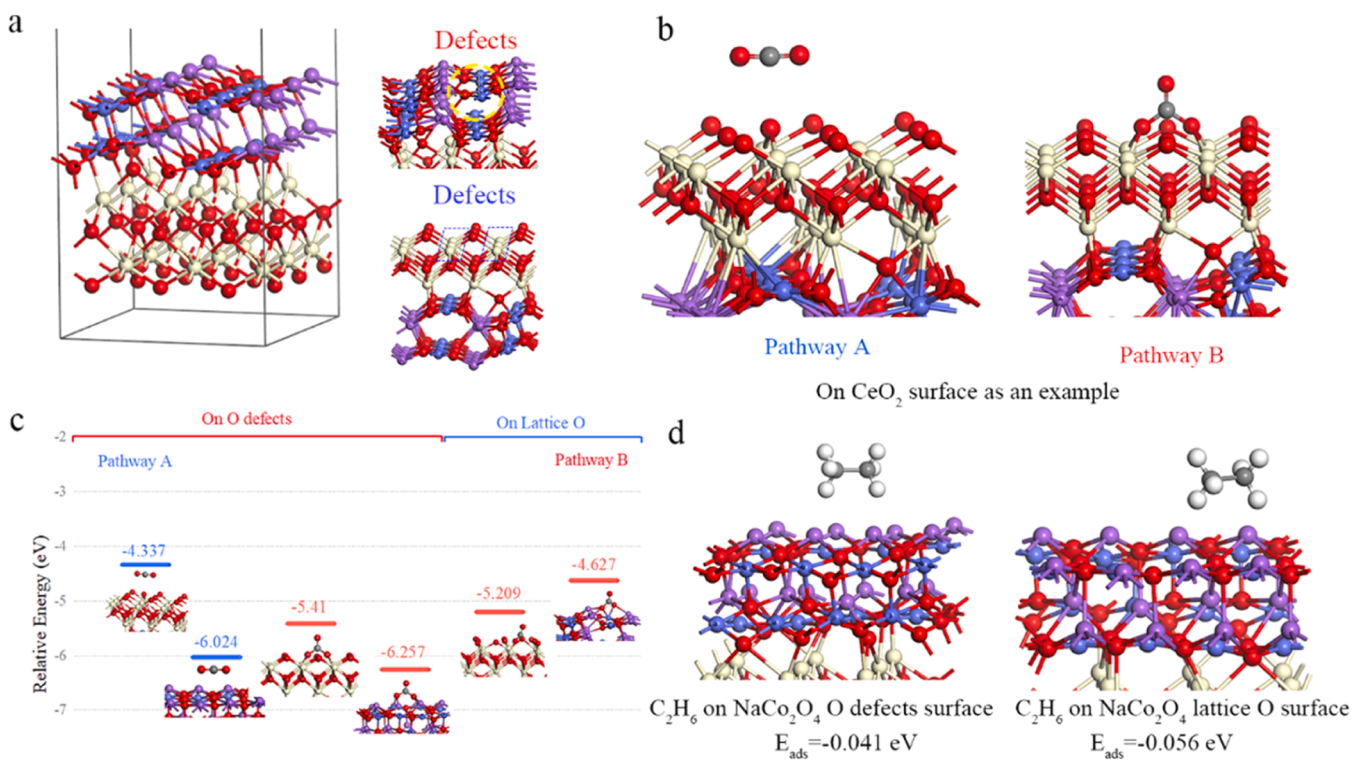


Fig. 5. (a) The structure of $2\text{NaCo}_2\text{O}_4/\text{CeO}_2$ in both crystal plane of (100). (b) Two pathways for CO_3^{2-} adsorption. (c) The CO_3^{2-} adsorption energy (E_{ads}) in lattice O surface and O defects surface by two pathways. (d) C_2H_6 adsorption energy (E_{ads}) in NaCo_2O_4 (100) surface.

lattice O of CeO₂ could also exist CO₃²⁻ OR. From all these results, in the overall CO₃²⁻ OR on 2NaCo₂O₄/CeO₂ surface, CeO₂ could indeed separate a portion since C₂H₆ OR could happen on NaCo₂O₄.

The adsorption energy of C₂H₆ on NaCo₂O₄ was calculated to investigate the competition of CO₃²⁻ OR and C₂H₆ OR. From Fig. 5d, the E_{ads} on lattice O is -0.056 eV, which is lower than that of O defects (-0.041 eV). Comparing with the E_{ads} of CO₃²⁻ OR, the number had a significant decline, which demonstrates that C₂H₆ OR is unfavorable. This proves that the CO₃²⁻ OR has a great effect on reducing the reaction energy barrier of C₂H₆.

4. Conclusion

We explored the incomplete oxidation of alkanes and chose ethane to be reactant as a example. In this process, we found a relationship between the electrolyte and target reactants and offered a solution to control this two reaction. In this study, the NaCo₂O₄ has a strong capability of both CO₃²⁻ OR and C₂H₆OR, to regulate these two reactions, CeO₂ was composited with NaCo₂O₄ to decline C₂H₆ OR. We found the best ratio of these two catalysts and converted C₂H₆ to 2-propanol and acetone. Furthermore, the changing process of catalysts was recorded and we found that the lattice O had a great increase and the O defects were declined. After comparing the capability of CO₃²⁻ OR and C₂H₆ OR, we confirmed that lattice O on NaCo₂O₄ was the active site for C₂H₆ OR and CO₃²⁻ OR mainly occurred on O defects. In addition, the relationship of these two reactions was inferred that the CO₃²⁻ OR could promote the C₂H₆ OR and must exist, however, excessive CO₃²⁻ OR could restrain the C₂H₆ OR. Moreover, the reaction pathway of C₂H₆ OR was inferred by in situ ATR-FTIR and the conclusions obtained before. DFT calculation was also verified these conclusion and speculated the mechanism of how CO₃²⁻ promote the target reaction. In conclusion, improving the performance of catalysts is not the best way in this competitive system, regulating the different reactions and find the balance is the key factor to achieve target reaction.

Funding Information

This work was supported by National Natural Science Foundation of China (U20A20130), Hebei Natural Science Foundation (B2021208033, B2022208040).

CRediT authorship contribution statement

Jiaqi Lv: Methodology, Formal analysis. **Xuan Liu:** Investigation, Formal analysis. **Xuerui Hao:** Methodology, Formal analysis. **Erhong Duan:** Writing – review & editing, Supervision, Resources, Funding acquisition. **Yubo Zhang:** Writing – original draft, Investigation, Formal analysis, Data curation. **Saifei Wang:** Writing – review & editing, Funding acquisition, Formal analysis.

Declaration of Competing Interest

The authors declare that they have no known competing financial interests or personal relationships that could have appeared to influence the work reported in this paper.

Data availability

No data was used for the research described in the article.

Appendix A. Supporting information

Supplementary data associated with this article can be found in the online version at doi:10.1016/j.apcatb.2024.124063.

References

- [1] Jeffrey J. Siirala, The impact of shale gas in the chemical industry, *AIChE J.* 60 (2014) 810–819.
- [2] D. Dogu, K.E. Meyer, A. Fuller, S. Gunduz, D.J. Deka, N. Kramer, A.C. Co, U. S. Ozkan, Effect of lanthanum and chlorine doping on strontium titanates for the electrocatalytically-assisted oxidative dehydrogenation of ethane, *Appl. Catal. B: Environ.* 227 (2018) 90–101.
- [3] X. Zhang, L. Ye, H. Li, F. Chen, K. Xie, Electrochemical dehydrogenation of ethane to ethylene in a solid oxide electrolyzer, *ACS Catal.* 10 (2020) 3505–3513.
- [4] Y. Bian, M. Kim, T. Li, A. Astaghiri, J.F. Weaver, Facile Dehydrogenation of Ethane on the IrO₂(110) Surface.
- [5] S.J. Cassady, R. Choudhary, N.H. Pinkowski, J. Shao, D.F. Davidson, R.K. Hanson, The thermal decomposition of ethane, *Fuel* 268 (2020) 117409.
- [6] X. He, Z. Li, H. Hu, J. Chen, L. Zeng, J. Zhang, W. Lin, C. Wang, Chemical looping conversion of ethane to ethanol via photo-assisted nitration of ethane, *Cell Rep. Phys. Sci.* 2 (2021) 100481.
- [7] J. Deng, S.-C. Lin, J. Fuller, J.A. Iñiguez, D. Xiang, D. Yang, G. Chan, H.M. Chen, A. N. Alexandrova, C. Liu, Ambient methane functionalization initiated by electrochemical oxidation of a vanadium (V)-oxo dimer, *Nat. Commun.* 11 (2020) 3686.
- [8] C. Kim, H. Min, J. Kim, J. Sul, J. Yang, J.H. Moon, NiO/ZnO heterojunction nanorod catalyst for high-efficiency electrochemical conversion of methane, *Appl. Catal. B: Environ.* 323 (2023) 122129.
- [9] J. Lee, S. Lee, C. Kim, J.S. Yoo, J.H. Moon, High-efficiency electrochemical methane conversion using Fe2O3-based catalysts assisted by thermochemical active oxygen, *Appl. Catal. B: Environ.* 344 (2024) 123633.
- [10] J. Li, L. Yao, D. Wu, Electrocatalytic methane oxidation to ethanol on iron-nickel hydroxide nanosheets, *Appl. Catal. B: Environ.* (2022) 316.
- [11] Z. Zhang, Y. Dong, C. Carlos, X. Wang, Surface ligand modification on ultrathin Ni(OH)₂ nanosheets enabling enhanced alkaline ethanol oxidation kinetics, *ACS Nano* 17 (2023) 17180–17189.
- [12] J. Ke, M. Chi, J. Zhao, Y. Liu, R. Wang, K. Fan, Y. Zhou, Z. Xi, X. Kong, H. Li, J. Zeng, Z. Geng, Dynamically reversible interconversion of molecular catalysts for efficient electrooxidation of propylene into propylene glycol, *J. Am. Chem. Soc.* 145 (2023) 9104–9111.
- [13] G. Kresse, D. Joubert, From ultrasoft pseudopotentials to the projector augmented-wave method, *Phys. Rev. B* 59 (1999) 1758.
- [14] J.P. Perdew, K. Burke, M. Ernzerhof, Generalized gradient approximation made simple, *Phys. Rev. Lett.* 77 (1996) 3865.
- [15] L. Xie, J. Cheng, T. Wang, X. Lu, Mechanical wear behavior between CeO₂(100), CeO₂(110), CeO₂(111), and silicon studied through atomic force microscopy, *Tribol. Int.* 153 (2021) 106616.
- [16] E.M. Jakubczyk, A. Mapp, C.C. Chung, C.L. Sansom, J.L. Jones, R.A. Dorey, Enhancing thermoelectric properties of NaCo₂O₄ ceramics through Na pre-treatment induced nano-decoration, *J. Alloy. Compd.* 788 (2019) 91–101.
- [17] F. Liu, S. Zhang, L. Wan, Y. Hao, J. Li, H. Wang, Z. Li, Q. Li, C. Cao, Attachment of facile synthesized NaCo₂O₄ nanodots to SiO₂ nanoflakes for sodium-rich boosted Pt-dominated ambient HCHO oxidation, *J. Hazard. Mater.* 458 (2023) 131969.
- [18] Z. Rao, K. Wang, Y. Cao, Y. Feng, Z. Huang, Y. Chen, S. Wei, L. Liu, Z. Gong, Y. Cui, L. Li, X. Tu, D. Ma, Y. Zhou, Light-reinforced key intermediate for anticoking to boost highly durable methane dry reforming over single atom Ni active sites on CeO₂, *J. Am. Chem. Soc.* (2023).
- [19] N. Spinner, W.E. Mustain, Electrochemical methane activation and conversion to oxygenates at room temperature, *ECS Trans.* 53 (2013) 1.
- [20] M. Ma, B.J. Jin, P. Li, M.S. Jung, J.I. Kim, Y. Cho, S. Kim, J.H. Moon, J.H. Park, Ultrahigh electrocatalytic conversion of methane at room temperature, *Adv. Sci.* (2017) 1700379.
- [21] M. Ma, C. Oh, J. Kim, J.H. Moon, J.H. Park, Electrochemical CH₄ oxidation into acids and ketones on ZrO₂:NiCo₂O₄ quasi-solid solution nanowire catalyst, *Appl. Catal. B: Environ.* 259 (2019) 118095.
- [22] C. Shan, Y. Zhang, Q. Zhao, K. Fu, Y. Zheng, R. Han, C. Liu, N. Ji, W. Wang, Q. Liu, Acid etching-induced in situ growth of λ -MnO₂ over CoMn spinel for low-temperature volatile organic compound oxidation, *Environ. Sci. Technol.* 56 (2022) 10381–10390.
- [23] X. Yue, X. Qin, Y. Chen, Y. Peng, C. Liang, M. Feng, X. Qiu, M. Shao, S. Huang, Constructing active sites from atomic-scale geometrical engineering in spinel oxide solid solutions for efficient and robust oxygen evolution reaction electrocatalysts, *Adv. Sci.* 8 (2021) 2101653.
- [24] M. Wang, N. Shang, W. Gao, X. Cheng, S. Gao, C. Wang, Anchoring Co on CeO₂ nanoflower as an efficient catalyst for hydrogenolysis of 5-hydroxymethylfurfural, *Fuel* 354 (2023) 129433.
- [25] C. Costentin, T.R. Porter, J.M.J. JotA.C.S. Saveant, Conduction and Reactivity in Heterogeneous-Molecular Catalysis: New Insights in Water Oxidation Catalysis by Phosphate Cobalt Oxide Films, 138 (2016) 5615–5622.
- [26] C. Pasquini, I. Zaharieva, D. Gonzalez-Flores, P. Chernev, M.R. Mohammadi, L. Guidoni, R.D.L. Smith, H.J.JotA.C.S. Dau, H/D Isotope Effects Reveal Factors Controlling Catalytic Activity in Co-Based Oxides for Water Oxidation, 141 (2019) 2938–2948.
- [27] A. Moysiadou, S. Lee, C.S. Hsu, H.M. Chen, X.J.JotA.C.S. Hu, Mechanism of Oxygen Evolution Catalyzed by Cobalt Oxyhydroxide: Cobalt Superoxide Species as a Key Intermediate and Dioxygen Release as a Rate-Determining Step, 142 11901–11914.
- [28] J. Huang, H. Sheng, R.D. Ross, J. Han, X. Wang, B. Song, S. Jin, Modifying redox properties and local bonding of Co₃O₄ by CeO₂ enhances oxygen evolution catalysis in acid, *Nat. Commun.* 12 (2021) 3036.

[29] J. Li, L. Yao, D. Wu, J. King, S.S.C. Chuang, B. Liu, Z. Peng, Electrocatalytic methane oxidation to ethanol on iron-nickel hydroxide nanosheets, *Appl. Catal. B: Environ.* 316 (2022) 121657.

[30] Z.-Y. Zhou, Q. Wang, J.-L. Lin, N. Tian, S.-G. Sun, In situ FTIR spectroscopic studies of electrooxidation of ethanol on Pd electrode in alkaline media, *Electrochim. Acta* 55 (2010) 7995–7999.

[31] M. Guo, P. Ma, L. Wei, J. Wang, Z. Wang, K. Zheng, D. Cheng, Y. Liu, H. Dai, G. Guo, E. Duan, J. Deng, Highly selective activation of C–H bond and inhibition of C–C bond cleavage by tuning strong oxidative Pd sites, *J. Am. Chem. Soc.* 145 (2023) 11110–11120.

[32] C. Barakat, P. Gravejat, O. Guaitella, F. Thevenet, A. Rousseau, Oxidation of isopropanol and acetone adsorbed on TiO₂ under plasma generated ozone flow: Gas phase and adsorbed species monitoring, *Appl. Catal. B: Environ.* 147 (2014) 302–313.

[33] T. Chen, S. Xu, T. Zhao, X. Zhou, J. Hu, X. Xu, C. Liang, M. Liu, W. Ding, Accelerating Ethanol Complete Electrooxidation via Introducing Ethylene as the Precursor for the C–C Bond Splitting, 62 (2023) e202308057.

[34] Y. Niu, Y. Guan, C. Long, C. Ren, J. Lu, C. Jin, P. Wang, X. Fan, H.-L. Xie, A universal strategy for achieving dual cross-linked networks to obtain ultralong polymeric room temperature phosphorescence, *Sci. China Chem.* 66 (2023) 1161–1168.

[35] J. Duan, S. Fan, X. Li, J. Wang, C. Bai, S. Yu, W. Ling, R. Tian, D. Zhang, Hollow AMn204-8 (A = Co, Zn, Ni) nanotube for direct photo-oxidation of methane to C1 and C2 alcohols at atmospheric pressure and room temperature, *Chem. Eng. J.* 485 (2024) 149904.

[36] P. Wang, R. Shi, Y. Zhao, Z. Li, J. Zhao, J. Zhao, G.I.N. Waterhouse, L.-Z. Wu, T. Zhang, Selective photocatalytic oxidative coupling of methane via regulating methyl intermediates over metal/ZnO nanoparticles, *Angew. Chem. Int. Ed.* 62 (2023) e202304301.

[37] B. Yu, L. Cheng, S. Dai, Y. Jiang, B. Yang, H. Li, Y. Zhao, J. Xu, Y. Zhang, C. Pan, X.-M. Cao, Y. Zhu, Y. Lou, Silver and copper dual single atoms boosting direct oxidation of methane to methanol via synergistic catalysis, *Adv. Sci.* 10 (2023) 2302143.

[38] X. Chen, M. Yu, Z. Yan, W. Guo, G. Fan, Y. Ni, J. Liu, W. Zhang, W. Xie, F. Cheng, J. Chen, Boosting Electrocatalytic Oxygen Evolution by Cation Defect Modulation via Electrochemical Etching, 3 (2021) 675–685.

[39] Y. Duan, S. Sun, Y. Sun, S. Xi, X. Chi, Q. Zhang, X. Ren, J. Wang, S.J.H. Ong, Y. Du, L. Gu, A. Grimaud, Z.J. Xu, Mastering surface reconstruction of metastable spinel oxides for better water oxidation, *Adv. Mater.* 31 (2019) 1807898.

[40] S. Wang, H. Li, M. He, X. Cui, L. Hua, H. Li, J. Xiao, L. Yu, N.P. Rajan, Z. Xie, D. Deng, Room-temperature conversion of ethane and the mechanism understanding over single iron atoms confined in graphene, *J. Energy Chem.* 36 (2019) 47–50.

[41] R. Yao, J.E. Herrera, L. Chen, Y.-H.C. Chin, Generalized mechanistic framework for ethane dehydrogenation and oxidative dehydrogenation on molybdenum oxide catalysts, *ACS Catal.* 10 (2020) 6952–6968.

[42] J.A. Keith, P.M. Henry, The mechanism of the Wacker reaction: a tale of two hydroxypalladations, *Angew. Chem. Int. Ed.* 48 (2009) 9038–9049.